Inorganic Chemistry
Forum Article
Cite This: Inorg. Chem. XXXX, XXX, XXX−XXX
pubs.acs.org/IC

Electronic Structure of Manganese Corroles Revisited: X-ray Structures, Optical and X-ray Absorption Spectroscopies, and Electrochemistry as Probes of Ligand Noninnocence

Sumit Ganguly,[†] Laura J. McCormick,[‡] Jeanet Conradie,[§] Kevin J. Gagnon,[‡] Ritimukta Sarangi,*[,∥] and Abhik Ghosh*[,†]

[†]Department of Chemistry, UiT—The Arctic University of Norway, Tromsø N-9037, Norway
[‡]Advanced Light Source, Lawrence Berkeley National Laboratory, Berkeley, California 94720-8229, United States
[§]Department of Chemistry, University of the Free State, Bloemfontein 9300, Republic of South Africa
[∥]Structural Molecular Biology (SMB), Stanford Synchrotron Radiation Lightsource (SSRL), SLAC National Accelerator Laboratory, Menlo Park, California 94306, United States

Supporting Information

ABSTRACT: Presented herein is a detailed multitechnique investigation of ligand noninnocence in $S = {}^{3}/_{2}$ manganese corrole derivatives at the formal Mn^{IV} oxidation state. The Soret maxima of Mn[T*p*XPC]Cl (T*p*XPC = *meso*-tris(*p*-X-phenyl)corrole, where X = CF$_3$, H, Me, and OMe) were found to red-shift over a range of 37 nm with increasing electron-donating character of X. For Mn[T*p*XPC]Ph, in contrast, the complex Soret envelopes were found to be largely independent of X. These observations suggested a noninnocent corrole$^{\bullet 2-}$-like ligand for the MnCl complexes and an innocent corrole^{3-} ligand for the MnPh complexes. Single-crystal X-ray structures of three Mn[T*p*XPC]Cl complexes revealed skeletal bond-length alternations indicative of a noninnocent corrole, while no such alternation was observed for Mn[T*p*OMePC]Ph. B3LYP density functional theory (DFT) calculations on Mn[TPC]Cl yielded strong spatial separation of the α and β spin densities, consistent with an antiferromagnetically coupled Mn^{III}-corrole$^{\bullet 2-}$ description. By comparison, relatively little spatial separation of the α and β spin densities was found for Mn[TPC]Ph, consistent with an essentially Mn^{IV}-corrole^{3-} description. X-ray absorption of near-edge spectroscopy (XANES) revealed a moderate blue shift of 0.6 eV for the Mn K-pre-edge of Mn[T*p*CF$_3$PC]Ph and a striking enhancement of the pre-edge intensity, relative to Mn[T*p*CF$_3$PC]Cl, consistent with a more oxidized, i.e., Mn^{IV}, center in Mn[T*p*CF$_3$PC]Ph. Time-dependent DFT calculations indicated that the enhanced intensity of the Mn K-pre-edge of Mn[T*p*CF$_3$PC]Ph results from the extra 3d$_{z^2}$ hole, which mixes strongly with the Mn 4p$_z$ orbital. Combined with similar results on Fe[TPC]Cl and Fe[TPC]Ph, the present study underscores the considerable potential of metal K-edge XANES in probing ligand noninnocence in first-row transition-metal corroles. Cyclic voltammetry measurements revealed highly negative first reduction potentials for the Mn[T*p*XPC]Ph series (∼−0.95 V) as well as large electrochemical HOMO-LUMO gaps of ∼1.7 V. The first reductions, however, are irreversible, suggesting cleavage of the Mn−Ph bond.

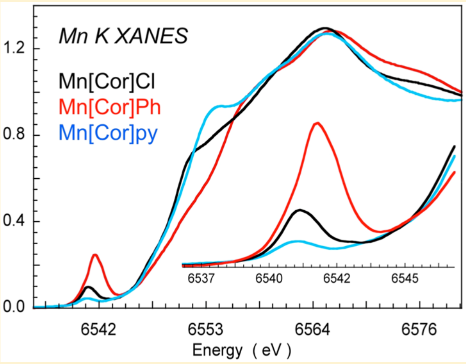

INTRODUCTION

In recent years, several families of iron[1] and copper[2−11] corroles have provided paradigmatic examples of noninnocent ligands; i.e., the corrole ligand in these complexes has substantial corrole$^{\bullet 2-}$ radical-dianion character.[12] Against this backdrop, this work presents a detailed analysis of ligand noninnocence in manganese corroles, for which the phenomenon has been less thoroughly explored. The study involved a multitechnique investigation of MnCl and MnPh (Ph = phenyl) *meso*-tris(*p*-X-phenyl)corrole (T*p*XPC) derivatives, where X = CF$_3$, H, Me, and OMe (Figure 1). Unlike for iron corroles, ^{1}H NMR and electron paramagnetic resonance (EPR) spectroscopies do not provide a detailed picture of the electron distribution in manganese corroles.[13,14] Accordingly, a major goal of the study was also to validate other key experimental methods, notably UV−vis spectroscopy, X-ray crystal structures, X-ray absorption spectroscopy (XAS), and electrochemistry, as probes of ligand noninnocence in manganese corroles.

Substituent effects of *meso*-aryl substituents on the Soret maximum have often provided the first indication of a noninnocent corrole in a given class of metallotriarylcorroles.

Special Issue: Applications of Metal Complexes with Ligand-Centered Radicals

Received: March 1, 2018

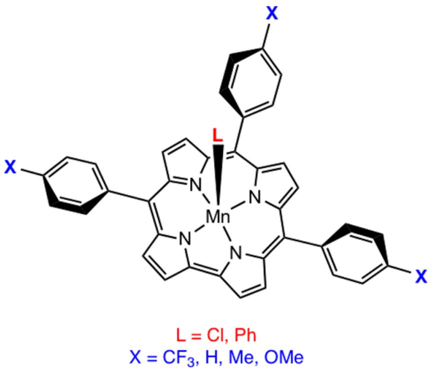

Figure 1. Manganese corroles studied in this work.

Thus, for noninnocent TpXPC derivatives, electron-donating X groups bring about distinct red shifts of the Soret maximum.[1−12] No such red shifts are observed for innocent metallotriarylcorroles.[15−21] The power of this simple optical probe has been dramatically underscored in recent reinvestigations of FeNO,[22] (μ-oxo)diiron,[23] and Co-PPh$_3$[24] corrole derivatives, which led us to reenvision these species as fundamentally noninnocent. Preliminary studies of a set of three Mn[TpXPC]Cl derivatives, where X = CF$_3$, H, and CH$_3$, revealed significant shifts of the Soret maxima, leading us to propose a Mn^{III}-corrole$^{\bullet 2-}$ formulation for these compounds.[13,25] Presented below is a comparative study of the Mn[TpXPC]Cl series, with X = CF$_3$, H, CH$_3$, and OMe, and the new series Mn[TpXPC]Ph.

Very recently, we have found a subtle but characteristic bond-length alternation in high-quality X-ray structures of noninnocent metallocorroles.[22,26,23,24] In view of the relative paucity of structurally characterized manganese corroles at the formal Mn^{IV} oxidation level, a number of single-crystal X-ray structure determinations were performed as part of this study. These fully substantiated the usefulness of high-quality X-ray structures as a potential probe of ligand noninnocence.

XAS has long been used as a probe of oxidation state, but the first applications to metallocorroles have only occurred recently.[27−29] For iron corroles, X-ray absorption near-edge spectroscopy (XANES) has provided an excellent probe of ligand noninnocence.[30] In this study, we have carried out a comparative XANES analysis of MnCl and MnPh corroles, again with excellent results.

Finally, we have addressed the question of whether electrochemical redox potentials are indicative of the innocent or noninnocent character of a given class of metallocorroles.

Throughout, density functional theory (DFT) calculations[31,32] have helped to interpret and contextualize the experimental data, as described below.

■ RESULTS AND DISCUSSION

Synthesis of MnCl and MnPh Corroles. The Mn[TpXPC]Cl (X = CF$_3$, H, Me, and OMe) derivatives were synthesized following a previously reported procedure.[33] Interaction of free-base triarylcorroles with Mn(OAc)$_2$·4H$_2$O in N,N-dimethylformamide (DMF) at 165−170 °C for approximately 45 min, followed by column chromatography, yielded the pure manganese(III) corroles. The manganese(III) corroles were then subjected to aerial oxidation in the presence of 10% aqueous HCl, affording the MnCl corroles. The new complex Mn[TpOMePC]Cl was obtained in approximately 40% yield (relative to H$_3$[TpOMePC]) with no particular adjustment to the procedure.

Arylation of the MnCl corroles was also carried out following a published protocol.[34,35] Anhydrous dichloromethane solutions of Mn[TpXPC]Cl derivatives were treated with an excess of phenylmagnesium bromide under an inert atmosphere, leading to Mn[TpXPC]Ph corroles via ligand exchange. The optimum reaction time was found to be about 7−8 min; longer reaction times resulted in drastically reduced yields. The MnPh products were obtained in 33−42% yield after aerobic workup.

Both MnCl and MnPh corroles are only moderately stable and are best stored in a freezer at under −50 °C. Under aerobic conditions in solution, the MnPh corroles were found to decompose rapidly via Mn−Ph bond cleavage [as judged from electrospray ionization mass spectromety (ESI-MS) analyses], visibly changing in color from reddish-brown to yellowish-green in about 1 h. Thus, even column chromatography and preparative thin-layer chromatography (PLC) over ~30 min under aerobic conditions resulted in a significant loss of material due to decomposition. Warming and rigorous drying of the solids also led to decomposition, frustrating our attempts at obtaining accurate elemental analyses. Accordingly, the sample purity was ascertained primarily by means of rapid analytical thin-layer chromatography on short (~4 cm) silica gel strips and ESI-MS as well as, in a number of cases, single-crystal X-ray structures.

Optical Spectroscopy. As shown in Table 1 and Figure 2, the Soret maxima of the Mn[TpXPC]Cl series red-shift dramatically from X = CF$_3$ (423 nm) to X = OMe (460 nm) series, strongly suggesting a noninnocent corrole.[1,22−25] Extrapolating conclusions based on time-dependent DFT

Table 1. Soret Absorption Maxima (nm) of Mn-, Fe-, Cu-, and Au[TpXPC] Complexes in CH$_2$Cl$_2$

	p-substituent				
series	CF$_3$	H	Me	OMe	ref
Mn[TpXPC]Cl	423	433	442	460	this work
Mn[TpXPC]Ph	398	394	389	387	this work
Fe[TpXPC]Cl	401	410	419	426	1, 30
Fe[TpXPC]Ph	384	383	383	385	30
Fe[TpXPC](NO)	385	390	400	416	22
Cu[TpXPC]	407	410	418	434	2
Au[TpXPC]	419	418	420	420	20

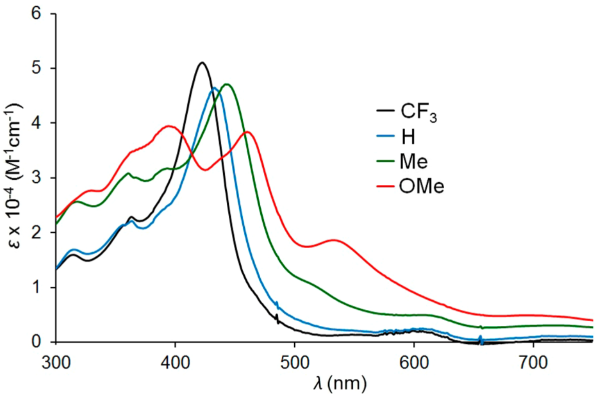

Figure 2. Electronic absorption spectra (in dichloromethane) of Mn[TpXPC]Cl derivatives.

(TDDFT) calculations on copper corroles,[36,37] we may plausibly assign the key substituent-sensitive feature in the complex Soret envelope to an aryl-to-corrole$^{\bullet 2-}$ ligand-to-ligand charge-transfer (LL′CT) transition. For the new compound Mn[T*p*OMePC]Cl, which has a pronounced split Soret band, this LL′CT transition may be reasonably assigned to the lower-energy peak with a maximum at 460 nm. For the Mn[T*p*XPC]Ph series (Figure 3), the Soret maxima drift somewhat erratically in the range 387−398 nm, but the overall peak envelopes do not move. Furthermore, the higher-wavelength shoulder of the Soret band, which all of the complexes exhibit and which presumably corresponds to the above-mentioned LL′CT transition, occurs at a fixed position, strongly suggesting an innocent corrole ligand. These conclusions are consistent with DFT(B3LYP/STO-TZP) calculations on Mn[TPC]Cl and Mn[TPC]Ph. Thus, note the much smaller minority spin populations on the corrole for Mn[TPC]Ph, consistent with an essentially Mn^{IV}-corrole^{3-} description (Figure 4), compared with Mn[TPC]Cl.[12] Importantly, these conclusions also nicely parallel those for FeCl and FePh triarylcorroles.[1,30]

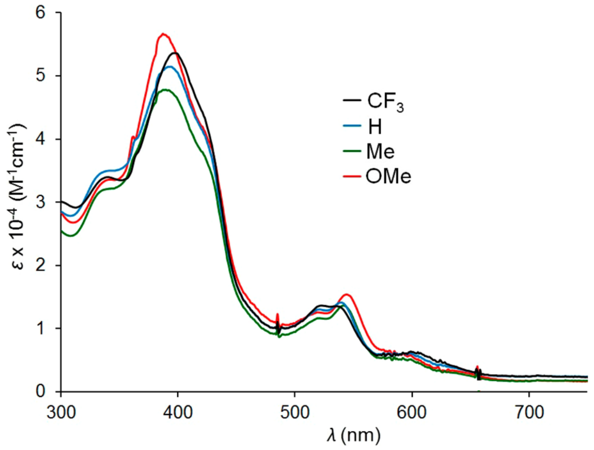

Figure 3. Electronic absorption spectra (in dichloromethane) of Mn[T*p*XPC]Ph derivatives.

As shown in Figure 5, the UV−vis spectra of MnCl and MnPh corroles differ markedly from those of manganese(III) corroles. Thus, the UV−vis spectrum of Mn[T*p*CF$_3$PC](py)$_n$ in dichloromethane exhibits a split Soret band, with two peaks of almost equal intensity at 408 and 430 nm. The characteristic Q band around 650 nm is thought to be indicative of a single axial pyridine ligand.[34,38−40]

X-ray Structures. Only a handful of manganese corroles have been structurally characterized until now.[14,34,35,41−43] Accordingly, a strong effort was made to determine single-crystal X-ray structures for the manganese corroles synthesized as part of this study. Five structures were successfully solved (Table 2). Key structural parameters of the MnCl and MnPh corroles are listed in Table 3 (along with literature comparisons) and illustrated in Figure 6. The structures underscore significant structural differences between the MnCl and MnPh corroles.

Thus, Table 3 shows that halogenomanganese corroles (including the previously reported structures MIKWOU,[41] TORMET,[44] YAWQES,[14] YAWQAO,[14] GIFJEL,[45] and XIDRUY[42]) exhibit significantly larger out-of-plane Mn−N$_4$ displacements than Mn-aryl corroles (including CISGUH[35] and CISHAO[35]). The higher displacements for the MnCl complexes facilitate antiferromagnetic coupling between the d_{z^2} electron of the high-spin Mn^{III} center and the "a_{2u}-type" corrole radical. The question of such a spin coupling does not arise for the d^3 Mn^{IV} center in Mn-aryl corroles.

Figure 6 reveals a small but distinct bond-length alternation in and around the bipyrrole unit of the three MnCl structures. An analogous bond-length alternation is also found for other structurally characterized halogenomanganese corroles (MIKWOU,[41] TORMET,[44] YAWQES,[14] YAWQAO,[14] GIFJEL,[45] and XIDRUY[42]) but is essentially nonexistent in the X-ray structure of Mn[T*p*OMePC]Ph (as well as CISGUH[35] and CISHAO[35]). We have recently shown that such a bond-length alternation is indicative of a corrole a_{2u}-type radical (allowing ourselves to use D_{4h} symbols for orbital symmetries that are standard for porphyrins).[22−24] DFT calculations also reproduce this difference in the skeletal bond-length alternation between Mn[TPC]Cl and Mn[TPC]Ph (Figure 4).

Interestingly, the X-ray structure of Mn[T*p*OMePC]Ph revealed two symmetry-distinct molecules, each existing as a slipped π-stacked dimer (Figure 7). Such π stacking is common for porphyrinoid structures. No such stacking, however, was observed for any of the three MnCl structures.

An attempt to structurally characterize a five-coordinate manganese(III) complex led to an X-ray structure of Mn[T*p*CF$_3$PC](py)$_2$ (Figure 8). Unsurprisingly for a high-spin manganese(III) complex, the Mn−N distances involving the axial pyridines were found to be long—2.4269(17) Å each—somewhat longer than that observed in the monopyridine complexes Mn[OEC]py (2.277 Å)[34] and Mn[T*p*NO$_2$PC]Cl (MIKWEK,[41] 2.385 Å). This finding is somewhat at odds with spectrophotometric titration[34,38,39] and mass spectrometric[46,47] studies, which indicate that the major species in solution in the presence of added pyridine is a five-coordinate manganese(III) corrole with a single axially bound pyridine. As described below and in the Supporting Information, however, XAS studies suggest that both monopyridine and bispyridine adducts may coexist, depending on the exact conditions.

XAS. Figure 9 depicts the Mn K-edge XAS data for the solid-state compounds Mn[T*p*CF$_3$PC]Cl, Mn[T*p*CF$_3$PC]Ph, and Mn[T*p*CF$_3$PC](py)$_n$ (n = 1−2); the inset shows an expanded view of the pre-edge region. The metal K-pre-edge spectra result from 1s-to-3d electric-dipole-forbidden, quadrupole-allowed transitions, and their energy positions and intensity patterns are strongly modulated by changes in the electronic structure. A comparative study of the pre-edge region, among closely related molecular systems, can provide important insight into electronic-structural differences. The K-pre-edge energy of first-row transition metal complexes is strongly affected by the overall ligand-field strength, and the pre-edge can gain intensity via two mechanisms: (1) an increase in the number of metal 3d holes and (2) an increase in metal 3d−4p mixing (associated with a decrease in centrosymmetry).[48,49] These general rules are expected to apply well to the structurally similar, square-pyramidal complexes examined here, which have the same TPC ligand as the dominant contributor to the overall ligand field.[50]

The expanded Mn K-pre-edge region (Figure 9, inset) shows that, upon going from the genuine manganese(III) species Mn[T*p*CF$_3$PC](py)$_n$ (n = 1−2) to Mn[T*p*CF$_3$PC]Cl, the intensity-weighted average energy (IWAE) position of the pre-edge increases slightly from 6540.6 to 6540.8 eV and the total intensity increases from 0.12 to 0.25 units, respectively. The modest increases in the pre-edge energy and intensity are

DOI: 10.1021/acs.inorgchem.8b00537
Inorg. Chem. XXXX, XXX, XXX−XXX

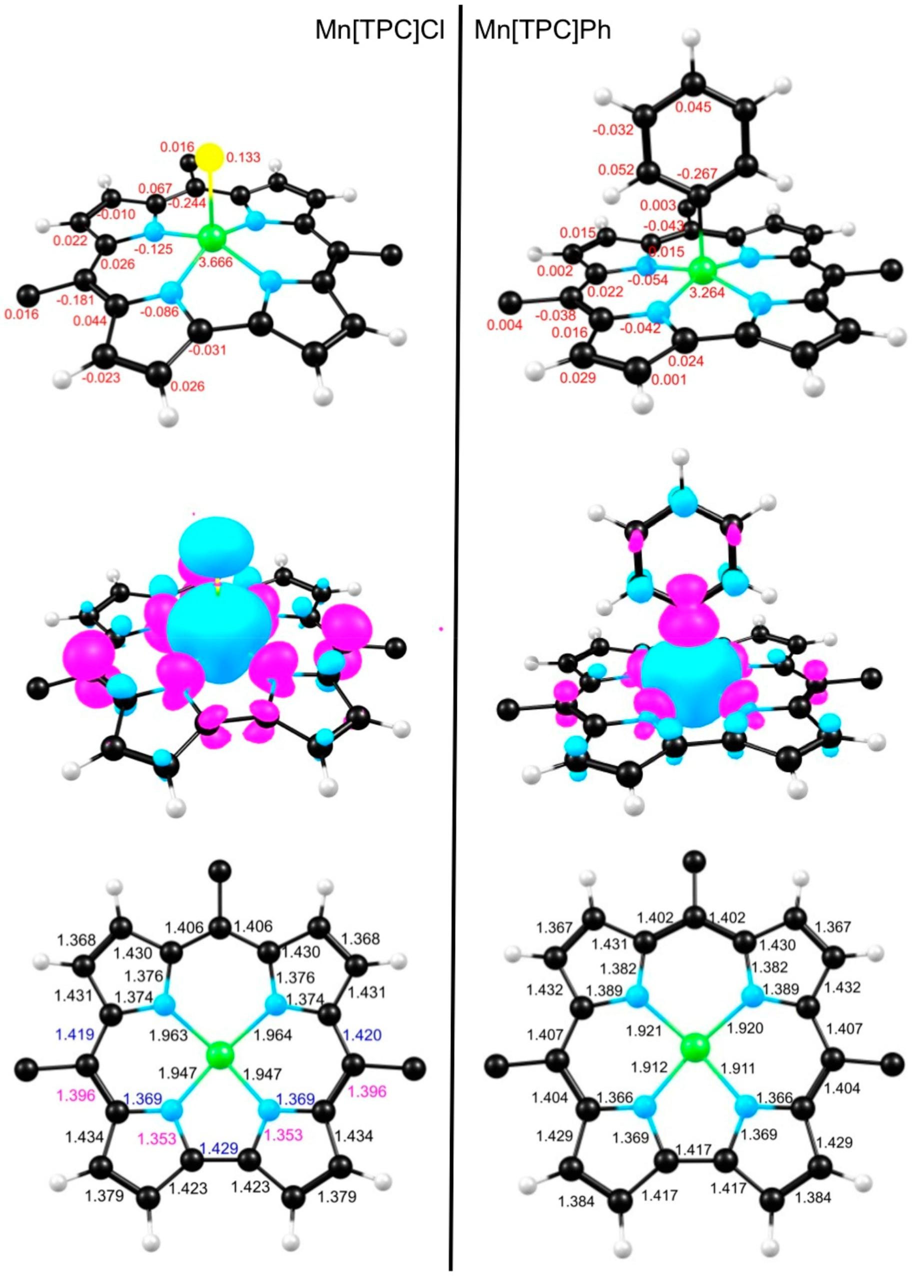

Figure 4. Comparative B3LYP/STO-TZP results for Mn[TPC]Cl and Mn[TPC]Ph. Top: Mulliken spin populations. Middle: Excess majority (cyan) and minority (magenta) spin densities plotted with a contour of 0.03 e/Å^3. Bottom: Skeletal bond distances (Å). Bond-length alternations are indicated in color for Mn[TPC]Cl. *meso*-Phenyl groups have been omitted for clarity.

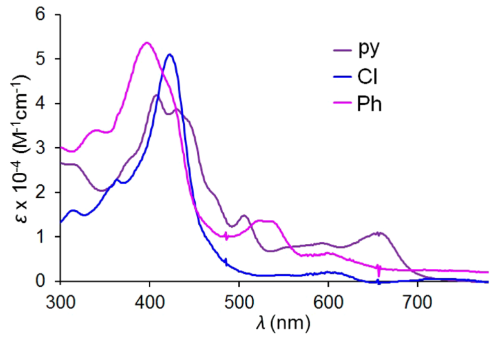

Figure 5. Comparative electronic absorption spectra (in dichloromethane) of the Mn[T*p*CF$_3$PC](L) complexes (L = py, Cl, and Ph).

consistent with a Mn^{III} center in both complexes, i.e., with a Mn^{III}(S=2)-corrole$^{\bullet 2-}$ electronic description for Mn-[T*p*CF$_3$PC]Cl. By comparison, the pre-edge energy position of Mn[T*p*CF$_3$PC]Ph is significantly blue-shifted and occurs at 6541.4 eV. The large increase in the pre-edge energy position is also accompanied by a dramatic increase in the pre-edge intensity (0.62 units). These results indicate either a significant increase in metal 3d−4p mixing in Mn[T*p*CF$_3$PC]Ph relative to Mn[T*p*CF$_3$PC]Cl or oxidation of the Mn center, which would lead to a manganese(IV) species with an additional d$_{z^2}$ hole.[30] To delineate the role of these two factors, DFT calculations with full geometry optimizations were carried out on the above three compounds. Figure 10, which depicts the unoccupied molecular orbital (MO) energy levels contributing to the Mn pre-edge region (see Figures S7 and S8 and Table S1

Table 2. Crystallographic Data for the Manganese Corroles Analyzed in This Work

	Mn[T*p*MePC]Cl	Mn[TPC]Cl	Mn[T*p*CF$_3$PC]Cl	Mn[T*p*OMePC]Ph	Mn[T*p*CF$_3$PC](py)$_2$
chemical formula	$C_{40}H_{29}ClMnN_4$	$C_{37}H_{23}ClMnN_4$	$C_{40}H_{20}ClF_9MnN_4$	$C_{46}H_{34}O_3N_4Mn$	$C_{50}H_{30}F_9MnN_6$
formula mass	656.06	613.98	817.99	745.71	940.74
cryst syst	monoclinic	monoclinic	triclinic	triclinic	monoclinic
space group	$P2_1/n$	$P2_1/n$	$P\bar{1}$	$P\bar{1}$	$C2/c$
λ (Å)	1.0332	0.7293	0.7749	0.7749	0.7749
a (Å)	15.8442(9)	8.2864(5)	8.2998(9)	10.1014(3)	18.3531(9)
b (Å)	12.4846(7)	15.8843(10)	11.6142(13)	13.6476(4)	16.7778(8)
c (Å)	16.5813(9)	21.0546(13)	18.151(2)	25.4568(8)	14.4477(7)
α (deg)	90	90	96.535(3)	94.755(2)	90
β (deg)	111.797(2)	90.063(3)	91.747(3)	95.107(2)	113.778(3)
γ (deg)	90	90	100.883(3)	90.353(2)	90
Z	4	4	2	4	4
Z'	1		1	2	0.5
V (Å^3)	3045.4(3)	2771.3(3)	1704.6(3)	3483.18(18)	4071.2(4)
temp (K)	100(2)	100(2)	100(2)	100(2)	100(2)
density (g/cm^3)	1.431	1.472	1.594	1422	1.535
measured reflns	26122	49491	19570	62858	26941
unique reflns	8496	8503	6235	12791	6233
parameters	418	408	561	979	324
restraints	0	33	50	0	0
R_{int}	0.0544	0.0616	0.0543	0.0638	0.0368
θ range (deg)	2.208−47.232	1.315−31.483	1.961−28.977	2.207−27.894	1.871−33.655
R_1, wR_2 (all data)	0.1126, 0.2080	0.0397, 0.0899	0.0850, 0.1205	0.0479, 0.1174	0.0641, 0.1547
S(GOF) (all data)	1.324	1.083	1.148	1.046	1.055
max/min residual density (e/Å^3)	0.808/−0.954	0.450/−0.304	0.649/−0.618	0.469/−0.482	3.203/−0.694

Table 3. Selected Crystallographic Geometry Parameters for Manganese Corroles at the Formal Mn^{IV} Oxidation State

complex	CCSD	chemical name	d(M−N$_{1/4}$)$_{ave}$	d(M−N$_{2/3}$)$_{ave}$	d(M−L$_{ax}$)	d(M−N$_4$)	ref
Mn[Et$_4$Me$_2$EtAc$_2$C]Cl	TORMET	chloro-7,8,12,13-tetraethyl-2,18-bis[2-(methoxycarbonyl)ethyl]-3,17-dimethylcorrolatomanganese, acetonitrile solvate	1.942	1.918	2.338	0.407	44
Mn[TPFPC]Cl	YAWQES	chloro-5,10,15-tris(pentafluorophenyl)corrolatomanganese, benzene solvate	1.940	1.924	2.312	0.427	14
Mn[T*p*NO$_2$PC]Cl	MIKWOU	chloro-5,10,15-tris(4-nitrophenyl)corrolatomanganese, dichloromethane solvate	1.931	1.919	2.284	0.429	41
Mn[T*p*MePC]Cl		chloro-5,10,15-tris(4-methylphenyl)corrolatomanganese	1.930	1.918	2.295	0.374	this work
Mn[TPC]Cl		chloro-5,10,15-triphenylcorrolatomanganese	1.939	1.920	2.284	0.410	this work
Mn[T*p*CF$_3$PC]Cl		chloro-5,10,15-tris(4-trifluoromethylphenyl)corrolatomanganese	1.934	1.914	2.287	0.406	this work
Mn[TPFPC]Br	YAWQAO	bromo-5,10,15-tris(pentafluorophenyl)corrolatomanganese, benzene solvate	1.936	1.915	2.428	0.416	14
Mn[Et$_8$BTC]I	GIFJEL	iodo-2,3,7,8,12,13,17,18-octaethyl-5,15-bis(4-methylphenyl)corrolatomanganese	1.938	1.918	2.633	0.361	45
Mn[Et$_8$DPhC]I	XIDRUY	iodo-2,3,7,8,12,13,17,18-octaethyl-5,15-diphenylcorrolatomanganese	1.945	1.922	2.663	0.380	42
Mn[Et$_8$Me$_2$C]Ph	CISGUH	phenyl-2,3,8,12,17,18-hexaethyl-7,13-dimethylcorrolatomanganese	1.902	1.881	2.019	0.285	35
Mn[Et$_6$Me$_2$C](4-C$_6$H$_4$Br)	CISHAO	4-bromophenyl-2,3,8,12,17,18-hexaethyl-7,13-dimethylcorrolatomanganese	1.900	1.897	2.019	0.247	35
Mn[T*p*OMePC]Ph Molecule 1		phenyl-5,10,15-tris(4-methoxyphenyl)corrolatomanganese	1.905	1.892	2.025	0.291	this work
Mn[T*p*OMePC]Ph Molecule 2		phenyl-5,10,15-tris(4-methoxyphenyl)corrolatomanganese	1.902	1.901	2.021	0.279	this work

for additional details), shows that the lowest unoccupied majority-spin MO of Mn[T*p*CF$_3$PC]Cl is essentially a "porphyrin a$_{2u}$-type" corrole MO, with only a small contribution from the Mn center, whereas the corresponding MO in Mn[T*p*CF$_3$PC]Ph is Mn 3d$_{z^2}$-based. The availability of this additional hole, which mixes strongly with the Mn 4p$_z$ orbital, would thus appear to be primarily responsible for the dramatic increase in the pre-edge intensity in Mn[T*p*CF$_3$PC]-Ph. This assignment was explicitly confirmed by TDDFT calculations, which did a good job of simulating the intensity profile of the pre-edge region of the three complexes in question (Table 4 and Figure 11).

The above manganese complexes make for an interesting comparison with Fe[TPC]Cl and Fe[TPC]Ph, which we recently investigated with a combination of spectroscopic and theoretical methods.[30] Thus, Fe[TPC]Cl and Fe[TPC]Ph have been described as Fe^{III}(S=$^3/_2$)-corrole$^{\bullet 2-}$ and Fe^{IV}(S=1)-corrole^{3-}, respectively, which mirrors analogous descriptions

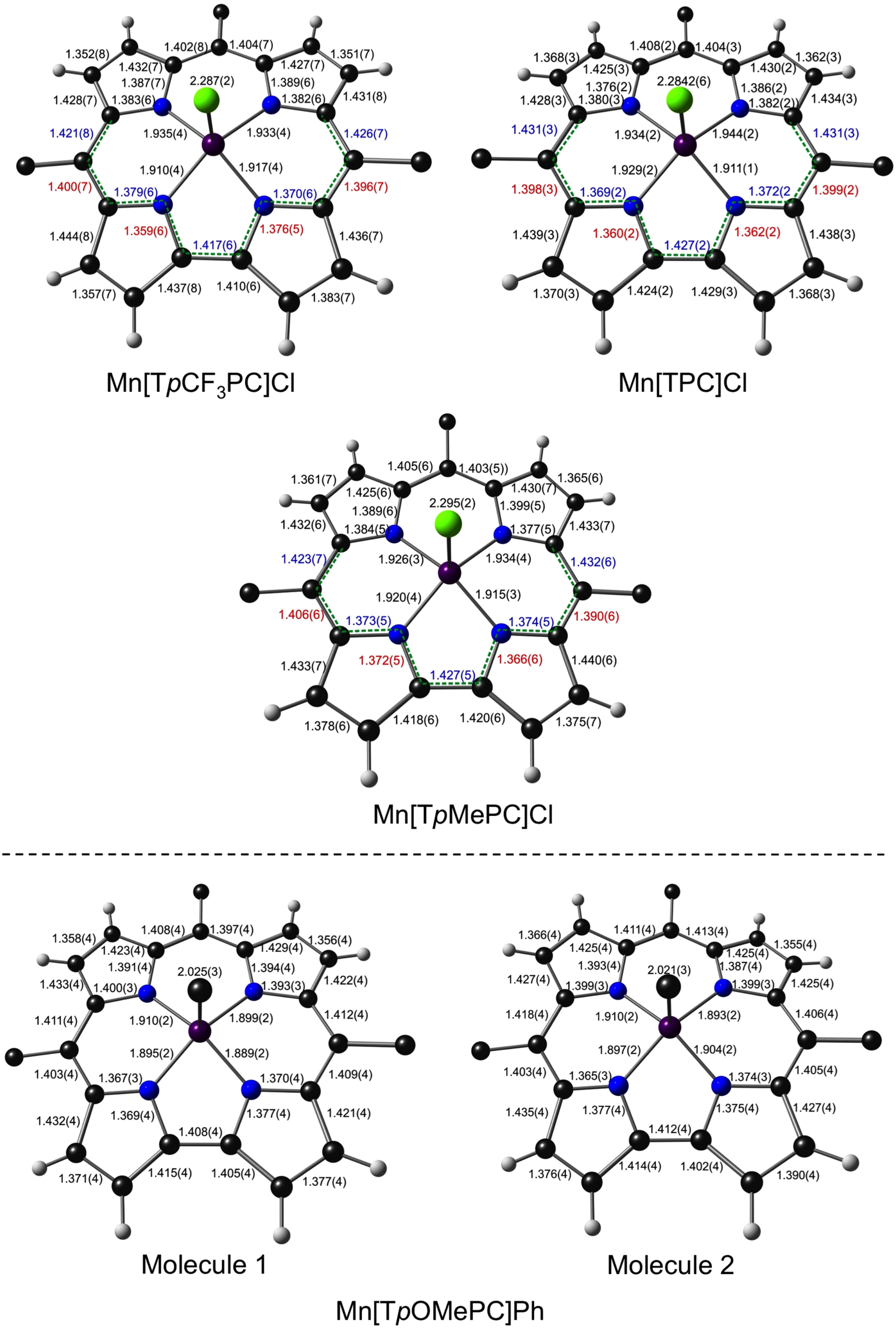

Mn[T*p*CF_3PC]Cl

Mn[TPC]Cl

Mn[T*p*MePC]Cl

Molecule 1

Molecule 2

Mn[T*p*OMePC]Ph

Figure 6. Selected crystallographic geometry parameters (Å) for MnCl and MnPh corroles studied in this work. In the top three structures, longer and shorter bond lengths are indicated in blue and red, respectively.

for their manganese counterparts. Moreover, the lowest unoccupied majority-spin MOs of Fe[TPC]Cl and Fe[TPC]Ph are corrole "a_{2u}"- and Fe $3d_{z^2}$-based, respectively, which explains the very similar trends in the pre-edge energy positions

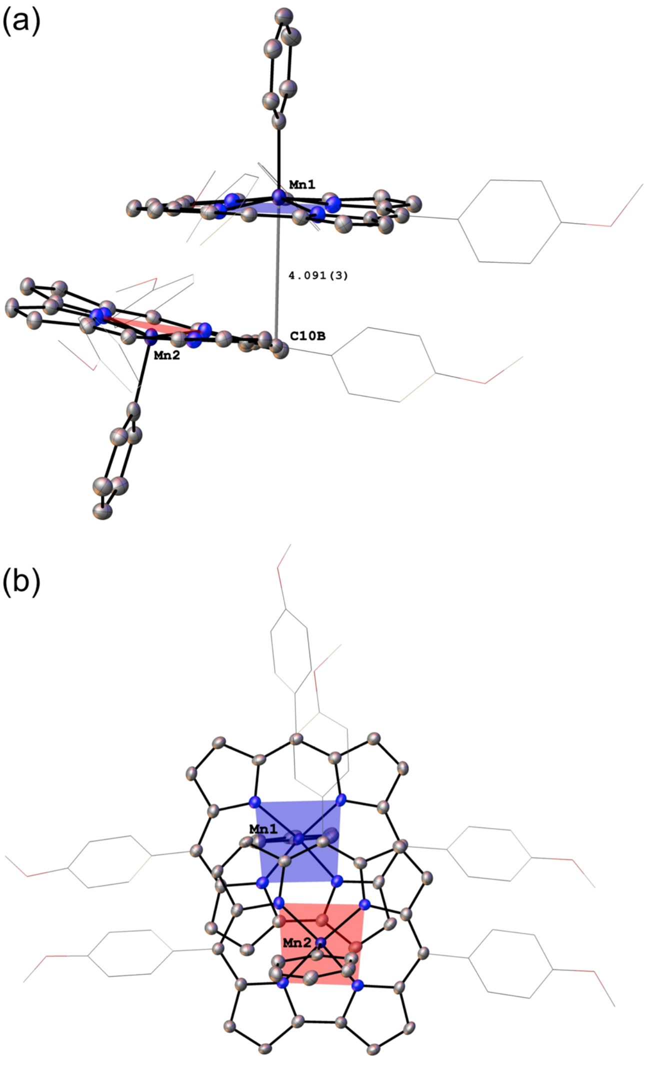

Figure 7. Two views of π-stacking interactions of Mn[T*p*OMePC]Ph.

and intensities for the two metals. The energy-shifted comparison depicted in Figure 12 is in full accord with this picture, underscoring the usefulness of metal K-pre-edges as a source of detailed electronic structural information.

Electrochemistry. The first oxidation potentials of the Mn[T*p*XPC]Cl series occur in the range 0.93−1.17 V versus the saturated calomel electrode (SCE) and are nearly identical to those observed for Fe[T*p*XPC]Cl (Figure 13 and Table 5). The first oxidation potential of the Mn[T*p*XPC]Ph series is slightly lower, by about 250 mV (Figure 13 and Table 4). Roughly speaking, the first oxidation potentials of all metal-lotriarylcorroles hover around +1.0 V (Table 4).[51] In contrast, the first reduction potentials vary considerably among different metallocorrole families, as described below.

The first reduction potentials of both the Mn[T*p*XPC]Cl and Fe[T*p*XPC]Cl series occur at around 0.1 ± 0.1 V, which corresponds to an electrochemical highest occupied molecular orbital (HOMO)−lowest unoccupied molecular orbital (LUMO) gap (defined as the difference between the first oxidation potential and the first reduction potential) of about 1.0 V. By comparison, the electrochemical HOMO−LUMO gaps of metallocorroles with redox-inactive metal centers such as Au,[20] $Os^{VI}N$,[17] and $Re^{V}O$[16] are approximately twice as large, 2.0−2.2 V.[52] It is reasonable to assume that the similar reduction potentials reflects similar reduction processes for the two metals:

$$\text{Cl-M}^{\text{III}}\text{-corrole}^{\bullet 2-}/\text{Cl-M}^{\text{III}}\text{-corrole}^{3-}\quad (\text{M} = \text{Mn},\ \text{Fe})$$

Thin-layer spectroelectrochemical studies by Kadish and co-workers, which revealed sharp Q bands for electroreduced MnCl corroles,[33,34] are suggestive of a fully aromatic reduced state and thus are consistent with the above assignment.

In contrast, the first reduction potentials of Mn[T*p*XPC]Ph occur at dramatically more negative potentials, at −0.95 ± 0.05 V, relative to the MnCl and FeCl series and even the FePh series (Table 4). In other words, the MnPh corroles are much more thermodynamically resistant to one-electron reduction than FePh corroles, consistent with the widespread prevalence of many stable manganese(IV) complexes. A key difference between the two metals, however, is that one-electron reduction of the Mn[T*p*XPC]Ph series is irreversible (Figure 13),[34] whereas the Fe[T*p*XPC]Ph series reduces reversibly.[30] In other words, the reduced MnPh center is less stable than the reduced FePh center. This difference between the two metals may be related to B3LYP calculations, indicating a significantly higher minority spin density on the *ipso*-C of the σ-phenyl group in MnPh corroles (about −0.27 in Figure 4) than on the analogous C in FePh corroles (−0.15).[12] That, along with the fact that the Mn carries a majority spin population greater than 3.0 (Figure 4), strongly suggests that the Mn center has a degree of Mn^{III} character:

$$\text{Mn}^{\text{IV}}(\uparrow\uparrow\uparrow) - \text{Ph} \leftrightarrow \text{Mn}^{\text{III}}(\uparrow\uparrow\uparrow\uparrow) - \text{Ph}^{\bullet}(\downarrow)$$

An interesting question concerns whether redox potentials, by themselves, can provide a clue as to the ground-state innocence or nonnoncence of a given metallocorrole family. It may be tempting to interpret the present results as a "yes". The nonninnocent MnCl and innocent MnPh series reduce at very different potentials and exhibit very different electrochemical HOMO−LUMO gaps. In contrast, however, the reduction potentials and electrochemical HOMO−LUMO gaps of analogous FeCl and FePh corroles exhibit much more modest differences.[30] Great care therefore must be exercised in relating redox potentials to the innocence or noninnocence of the corrole ligand in the neutral complex.

■ CONCLUSION

The synthesis of the new series of manganese complexes, Mn[T*p*XPC]Ph (X = CF_3, H, Me, and OMe), has allowed an extensive multitechnique comparison with the Mn[T*p*XPC]Cl series and a detailed examination of the question of ligand noninnocence in the two series. While the Soret bands of the former series were found to exhibit only minor variations, the Soret maxima of the latter series were found to red-shift by 37 nm from X = CF_3 to X = OMe. These observations, which parallel analogous observations for iron corroles, suggested a noninnocent $\text{corrole}^{\bullet 2-}$ ligand for the MnCl complexes and an innocent corrole^{3-} ligand for the MnPh complexes. Single-crystal X-ray structures of multiple Mn[T*p*XPC]Cl complexes also revealed bond-length alternations characteristic of non-innocent metallocorroles; no such bond-length alternation was observed for Mn[T*p*OMePC]Ph. Spin-unrestricted DFT calculations yielded spin-density profiles consistent with an antiferromagnetically coupled $\text{Mn}^{\text{III}}\text{-corrole}^{\bullet 2-}$ description for Mn[TPC]Cl and a largely $\text{Mn}^{\text{IV}}\text{-corrole}^{3-}$ description for Mn[TPC]Ph, albeit with a degree of $\text{Mn}^{\text{III}}\text{−Ph}^{\bullet}$ character. The

DOI: 10.1021/acs.inorgchem.8b00537
Inorg. Chem. XXXX, XXX, XXX−XXX

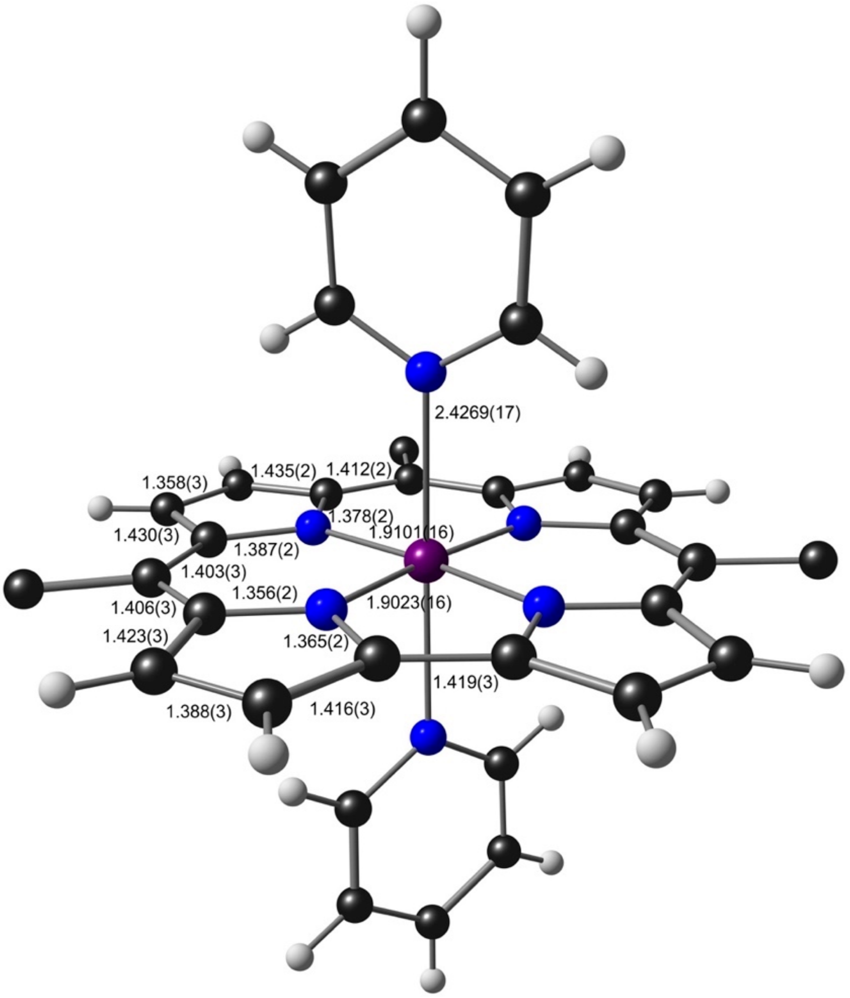

Figure 8. Selected symmetry-distinct geometry parameters (Å) for Mn[T*p*CF$_3$PC](py)$_2$. The *meso*-aryl groups have been deleted for clarity.

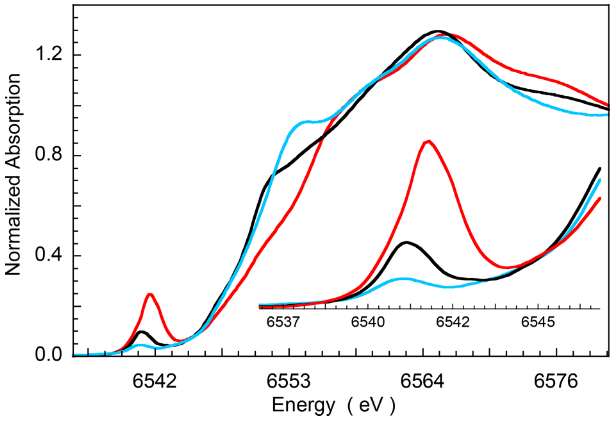

Figure 9. Normalized Mn K-edge XANES data for solid Mn[T*p*CF$_3$PC]Cl (black), Mn[T*p*CF$_3$PC]Ph (red), and Mn[T*p*CF$_3$PC](py)n (blue). The inset displays an expanded view of the pre-edge region.

calculations also reproduced the characteristic bond-length alternation for Mn[TPC]Cl. Although these results are not particularly surprising, their mutual consistency greatly bolsters our faith in the experimental and computational methods employed, viz., optical spectroscopy, X-ray crystallography, and DFT calculations, as probes of ligand noninnocence in corroles.

The much more negative reduction potentials of the MnPh complexes, relative to the MnCl complexes, also appear to be consistent with an innocent corrole ligand and a relatively stable Mn^{IV}Ph center. XANES, applied here for the first time to manganese corroles, nicely confirmed the above conclusions. Thus, compared with Mn[T*p*CF$_3$PC]Cl, the Mn K-pre-edge of Mn[T*p*CF$_3$PC]Ph was not only blue-shifted by 0.6 eV but also was dramatically more intense. DFT and TDDFT calculations showed that the enhanced intensity results from the extra d hole in MnPh compound. This hole, which corresponds to the LUMO, involves strong 3d$_{z^2}$−4p$_z$ mixing, the key factor underlying the dramatically enhanced pre-edge of Mn[TPC]Ph. Along with similar measurements on iron corroles, the present study underscores the considerable usefulness of XANES as a probe of metal-ion oxidation state, and thereby of ligand noninnocence, in metallocorroles.

■ EXPERIMENTAL SECTION

Materials. All reagents and solvents were used as purchased unless otherwise noted. Silica gel 150 (35−70 μm particle size, Davisil) was used as the stationary phase for flash chromatography, and silica gel 60 PLC plates (20 × 20 cm, 0.5 mm thick, Merck) were used for the final purification of the products. CHROMASOLV HPLC-grade *n*-hexane and dichloromethane were used as solvents for column chromatography. Phenylmagnesium bromide (3.0 M in diethyl ether, Sigma-Aldrich), Mn(OAc)$_2$·4H$_2$O (Merck), and pyridine (≥99%, Sigma-Aldrich) were used as received. For electrochemical measurements,

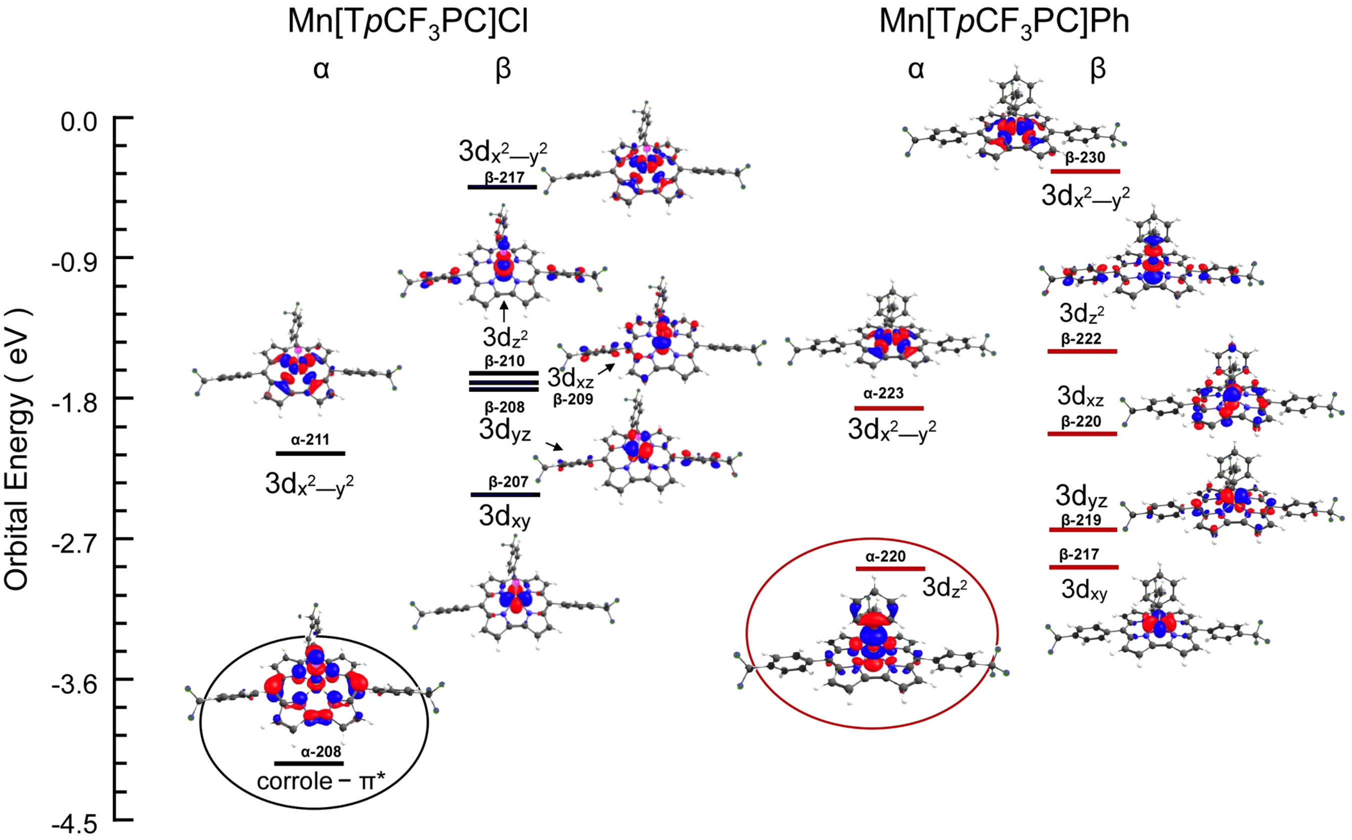

Figure 10. LUMO energy levels and contour plots for Mn[T*p*CF$_3$PC]Cl and Mn[T*p*CF$_3$PC]Ph. Only the Mn 3d-based MOs are shown, and ligand-based MOs have been omitted for clarity.

Table 4. Experimental and Calculated (TDDFT) IWAE Positions (eV) and Relative Intensities[a,b]

	Mn[T*p*CF$_3$PC](py)$_n$		Mn[T*p*CF$_3$PC]Cl		Mn[T*p*CF$_3$PC]Ph	
	calc	exp	calc	exp	calc	exp
IWAE	6372.2	6540.6	6372.3	6540.8	6372.7	6541.4
relative intensity	1.0	1.0	2	2.1	6.3	5.3

[a] The calculated and experimental intensities of solid Mn[T*p*CF$_3$PC](py)$_n$ have been set at 1.0 for the purpose of intercompound comparison. [b] For comparison with calculated TDDFT spectra, experimental IWAE positions obtained by fitting the data were fit with the *Peakfit* software (*Sigmaplot*).

commericially available anhydrous dichloromethane was predried with CaH$_2$, distilled, and stored over 3 Å molecular sieves. Tetrakis(*n*-butyl)ammonium perchlorate (Sigma-Aldrich), recrystallized three times from absolute ethanol, vacuum-dried at 40 °C for 2 days, and stored in a desiccator for at least 2 weeks, was used as the supporting electrolyte. The free-base corroles H$_3$[T*p*XPC] (X = CF$_3$, H, Me, and OMe) were synthesized as previously reported.[53]

Instrumentation. UV−vis spectra were recorded on an Agilent Cary 8454 UV−vis spectrophotometer in CH$_2$Cl$_2$. Cyclic voltammetry experiments were performed with an EG&G Princeton Applied Research model 263A potentiostat equipped with a three-electrode system consisting of a glassy carbon working electrode, a platinum wire counter electrode, and an SCE reference electrode. The reference electrode was separated from the bulk solution by a fritted-glass bridge filled with the solvent/supporting electrolyte mixture. All potentials were referenced to the SCE. A scan rate of 100 mV/s was used. The anhydrous dichloromethane solutions were purged with argon for at least 5 min prior to electrochemical measurements, and an argon blanket was maintained over the solutions during the measurements.

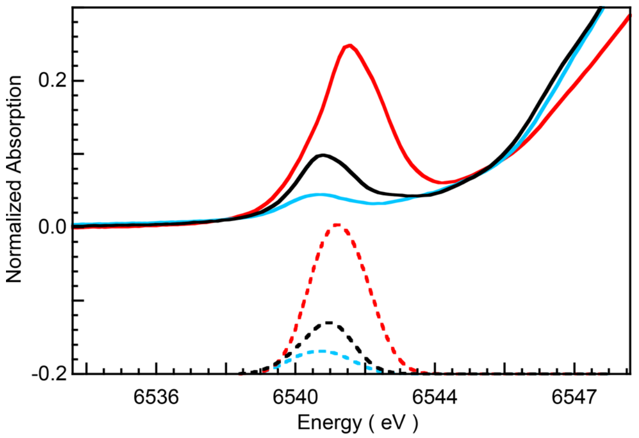

Figure 11. Comparison of the Mn K-pre-edge XAS data (solid lines) for solid Mn[T*p*CF$_3$PC](py)$_n$ (blue), Mn[T*p*CF$_3$PC]Cl (black), and Mn[T*p*CF$_3$PC]Ph (red) with the TDDFT-calculated spectra on their TPC analogues (dashed lines). The calculated spectra have been linearly upshifted by 168.2 eV. The calculated intensities have been scaled for graphical representation.

High-resolution mass spectrometry (HRMS) spectra were recorded on an LTQ Orbitrap XL spectrometer.

Synthesis of Mn[T*p*CF$_3$PC](py)$_n$. A 50 mL round-bottomed flask equipped with a magnetic stir-bar was charged with free-base tris(4-trifluoromethylphenyl)corrole (0.044 g, 0.06 mmol) dissolved in pyridine (15 mL). To this solution was added Mn(OAc)$_2$·4H$_2$O (10 equiv, 0.147 g, 0.60 mmol). The reaction flask was then fitted with a reflux condenser and heated on an oil bath at 105 °C with stirring for approximately 30 min, whereupon completion of metal insertion was confirmed by UV−vis spectroscopy and/or mass spectrometry. Upon

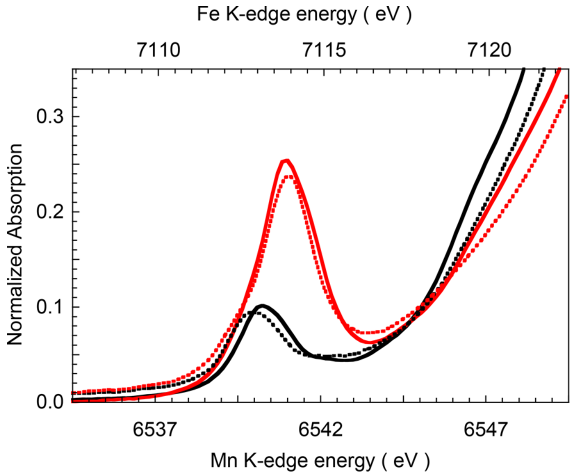

Figure 12. Comparison of the metal K-pre-edge XAS data for Mn[T*p*CF_3PC]Cl/Fe[TPC]Cl (black) and Mn[T*p*CF_3PC]Ph/Fe-[TPC]Ph (red), where the Mn and Fe data are indicated by solid and dashed lines, respectively.

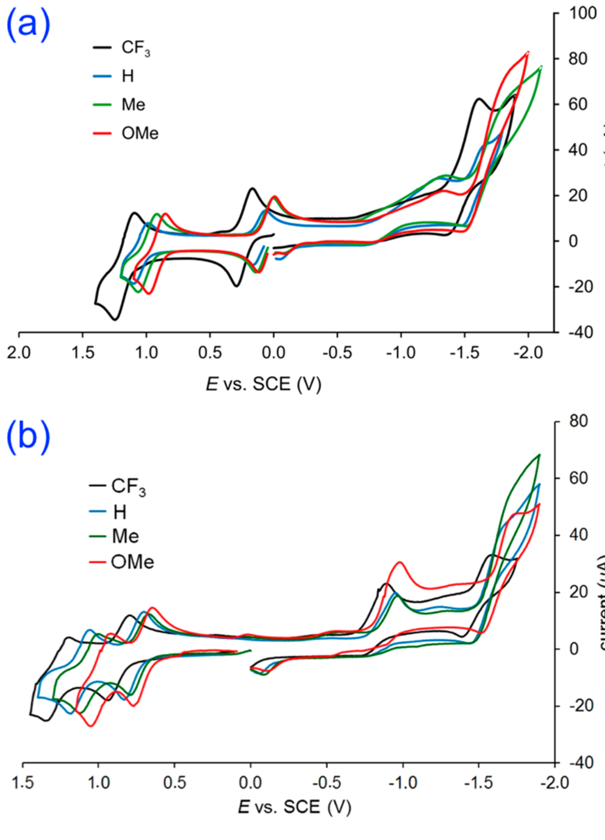

Figure 13. Cyclic voltammograms for the manganese corroles studied: Mn[T*p*XPC]Cl (top) and Mn[T*p*XPC]Ph (bottom).

cooling, the solution was rotary-evaporated to dryness under high vacuum. The resulting dark-greenish-brown residue was redissolved in a minimum volume of dichloromethane containing a couple of drops of pyridine and chromatographed on a silica gel column (12 cm height) with *n*-hexane/dichloromethane/pyridine (2:1:0.02) as the eluent. The front-running, green band was collected and identified as the title compound. Recrystallization from a mixture of approximately 5:1 *n*-hexane/dichloromethane with a few drops of pyridine afforded the solid product (0.0425 g, 0.049 mmol, 81.7% based on *n* = 1), which was used for XAS measurements. UV–vis [CH_2Cl_2; λ_{max}, nm ($\varepsilon \times 10^{-4}$, $M^{-1}cm^{-1}$)]: 408 (4.18), 430 (3.88), 506 (1.48), 658 (1.08).

Table 5. Electrochemical Data (V) for the Compounds Studied

series	X	E_{ox2}	E_{ox1}	E_{red1}	$E_{HOMO-LUMO}$	ref
Mn[T*p*XPC]Cl	CF_3		1.17	0.23	0.94	this work
	H		1.05	0.10	0.95	
	Me		1.00	0.07	0.93	
	OMe		0.93	0.06	0.87	
Mn[T*p*XPC]Ph	CF_3	1.27	0.86	−0.90[a]	1.76	this work
	H	1.13	0.77	−0.95[a]	1.72	
	Me	1.06	0.73	−0.97[a]	1.70	
	OMe	0.98	0.70	−0.99[a]	1.68	
Fe[T*p*XPC]Cl	CF_3		1.18	0.19	0.99	1, 30
	H		1.09	0.04	1.05	
	Me		1.05	0.00	1.05	
	OMe		0.97	0.03	0.94	
Fe[T*p*XPC](NO)	CF_3		0.98	−0.22	1.20	22
	H		0.86	−0.33	1.19	
	Me		0.84	−0.36	1.20	
	OMe		0.83	−0.37	1.20	
Fe[T*p*XPC]Ph	CF_3	1.29	0.92	−0.27	1.19	30
	H	1.20	0.82	−0.35	1.17	
	Me	1.14	0.78	−0.37	1.15	
	OMe	1.09	0.76	−0.39	1.15	
Cu[T*p*XPC]	CF_3		0.89	−0.08	0.97	2
	H		0.76	−0.20	0.96	
	Me		0.70	−0.23	0.93	
	OMe		0.65	−0.24	0.89	
Au[T*p*XPC]	CF_3		0.94	−1.29	2.23	20
	H	1.35	0.80	−1.38	2.18	
	Me	1.35	0.78	−1.42	2.20	
	OMe	1.32	0.76	−1.57	2.33	

[a] Peak potential for irreversible cathodic reduction.

HRMS (major isotopomers in the presence of a drop of pyridine; M = $C_{40}H_{20}N_4F_9Mn$; [M + py]$^+$): 861.1344 (exp), 861.1341 (calc). X-ray-quality crystals were obtained by the slow evaporation of a concentrated solution of the complex in 4:1 *n*-heptane/$CHCl_3$ containing a few drops of pyridine, over 3–4 weeks.

Synthesis of MnCl Corroles. A detailed procedure is described below for the synthesis of Mn[T*p*OMePC]Cl. A similar procedure was also followed for the synthesis of the other manganese complexes, except for details of the chromatographic purifications, which are specified separately.

Synthesis of Mn[T*p*OMePC]Cl. A 100 mL two-neck round-bottomed flask equipped with a magnetic stir-bar was charged with free-base tris(4-methoxyphenyl)corrole (0.1 g, 0.16 mmol) and DMF (40 mL). To the solution was added $Mn(OAc)_2{\cdot}4H_2O$ (10 equiv, 0.392 g, 1.6 mmol), and argon was bubbled through the solution for 5 min. The reaction flask was then fitted with a reflux condenser and heated on an oil bath at 165–170 °C with stirring for approximately 45 min. Completion of the reaction was confirmed by UV–vis spectroscopy and mass spectrometry. Upon cooling, the solution was rotary-evaporated to dryness to yield a dark-brownish-green residue. The residue was redissolved in a minimum volume of 1:1 dichloromethane/ethyl acetate and chromatographed on a silica gel column (8–10 cm height) with 1:1 *n*-hexane/ethyl acetate as the eluent. The front-running green band and the second reddish-brown band were collected and combined; these contained the initially formed manganese(III) corrole (as confirmed by ESI-MS).

The combined fraction was rotary-evaporated to dryness, and the residue was redissolved in dichloromethane (25 mL). The dichloromethane solution of manganese(III) corrole was treated with 10% aqueous HCl (3 × 25 mL), washed twice with distilled water, dried over anhydrous Na_2SO_4, and filtered, and the filtrate was rotary-evaporated under vacuum to yield a dark-reddish-brown residue. The residue was redissolved in a minimum volume of dichloromethane and chromatographed on a silica gel column (10 cm height) with dichloromethane and subsequently with 1:0.01 dichloromethane/methanol as the eluent. The reddish-brown band was collected and identified as pure Mn[T*p*OMePC]Cl (0.044 g, 0.062 mmol, 39% yield relative to free-base H_3[T*p*OMePC]). UV−vis [CH_2Cl_2; λ_{max}, nm ($\varepsilon \times 10^{-4}$, $M^{-1}cm^{-1}$)]: 330 (2.77), 394 (3.95), 460 (3.84), 533 (1.86). HRMS (major isotopomer; $[M]^-$):[54] 703.1314 (expt), 703.1314 (calc).

Synthesis of Mn[T*p*MePC]Cl. Silica gel column chromatography with dichloromethane and subsequently with 1:0.005 dichloromethane/methanol as the eluent afforded the pure product (0.061 g, 0.09 mmol, 53% relative to H_3[T*p*MePC]). UV−vis [CH_2Cl_2; λ_{max}, nm ($\varepsilon \times 10^{-4}$, M^{-1} cm^{-1})]: 318 (2.56), 361 (3.08), 442 (4.71). HRMS (major isotopomer; $[M]^-$): 655.1467 (expt), 655.1467 (calc). X-ray-quality crystals were obtained by the slow evaporation of a concentrated solution of the complex in 4:1 *n*-hexane/dichloromethane, over 2 weeks.

Synthesis of Mn[TPC]Cl. Silica gel column chromatography with dichloromethane and subsequently with 1:0.005 dichloromethane/methanol (200 mL) as the eluent afforded the pure product (0.053 g, 0.086 mmol, 45% relative to H_3[TPC]). UV−vis [CH_2Cl_2; λ_{max}, nm ($\varepsilon \times 10^{-4}$, M^{-1} cm^{-1})]: 315 (1.69), 363 (2.21), 433 (4.64). HRMS (major isotopomer; $[M]^-$): 613.1000 (expt), 613.0997 (calc). X-ray-quality crystals were obtained by the slow evaporation of a concentrated solution of the complex in 3:1 *n*-hexane/dichloromethane, over almost 2 weeks.

Synthesis of Mn[T*p*CF$_3$PC]Cl. Silica gel column chromatography with dichloromethane (3 × 500 mL) and subsequently with 1:0.005 dichloromethane/methanol (100 mL) as the eluent afforded the pure product (0.062 g, 0.076 mmol, 54% relative to H_3[T*p*CF_3PC]). UV−vis [CH_2Cl_2; λ_{max}, nm ($\varepsilon \times 10^{-4}$, M^{-1} cm^{-1})]: 314 (1.59), 363 (2.29), 423 (5.10). HRMS (major isotopomer; $[M]^-$): 817.0612 (expt), 817.0619 (calc). X-ray-quality crystals were obtained by the slow evaporation of a concentrated solution of the complex in 4:1 *n*-heptane/$CHCl_3$, over 3 weeks.

Synthesis of MnPh Corroles. A detailed procedure is described below for the synthesis of Mn[T*p*OMePC]Ph. A similar procedure was also followed for the synthesis of the other manganese complexes, except for details of the chromatographic purifications, which are specified separately.

Synthesis of Mn[T*p*OMePC]Ph. A 50 mL round-bottomed flask equipped with a magnetic stir-bar was charged with Mn[T*p*OMePC]Cl (0.04 g, 0.057 mmol). Anhydrous dichloromethane (15 mL) was added with a syringe under argon, and the mixture was stirred under argon for 5 min. Phenylmagnesium bromide (114 μL, 6 equiv) was then added with a syringe, and the mixture was stirred under argon for 7−8 min. The solution was then quenched with an excess of distilled water and extracted with dichloromethane. The organic fraction was dried with anhydrous $MgSO_4$ and filtered, and the filtrate was evaporated to dryness on a rotary evaporator under vacuum. The dark-brown residue obtained was redissolved in a minimum volume of dichloromethane and chromatographed on a silica gel column with 1:1 *n*-hexane/dichloromethane as the eluent. The product eluted as an intense dark-red band, which was collected and evaporated to dryness. Final purification was carried out with PLC using 1:2 *n*-hexane/dichloromethane as the eluent. The front-running red band contained pure Mn[T*p*OMePC]Ph (0.014 g, 33%). UV−vis [CH_2Cl_2; λ_{max}, nm ($\varepsilon \times 10^{-4}$, $M^{-1}cm^{-1}$)]: 341 (3.35), 387 (5.67), 429(sh) (3.8), 519 (1.26), 544 (1.54). HRMS (major isotopomer; $[M]^+$): 745.2009 (expt), 745.2006 (calc). Needle-shaped, X-ray-quality crystals were obtained by the slow diffusion of MeOH vapor into a concentrated $CHCl_3$ solution of the complex, over 1 week.

Synthesis of Mn[T*p*MePC]Ph. Silica gel column chromatography with 3:1 *n*-hexane/dichloromethane followed by PLC with 3:2 *n*-hexane/dichloromethane as the eluent afforded pure Mn[T*p*MePC]Ph (0.0156 g, 37%). UV−vis [CH_2Cl_2; λ_{max}, nm ($\varepsilon \times 10^{-4}$, M^{-1} cm^{-1})]: 341 (3.21), 389 (4.8), 521 (1.16), 542 (1.36). HRMS (major isotopomer; $[M]^+$): 697.2150 (expt), 697.2158 (calc).

Synthesis of Mn[TPC]Ph. Silica gel column chromatography with 3:1 *n*-hexane/dichloromethane followed by PLC with 2:1 *n*-hexane/dichloromethane as the eluent afforded pure Mn[TPC]Ph (0.018 g, 42%). UV−vis [CH_2Cl_2; λ_{max}, nm ($\varepsilon \times 10^{-4}$, M^{-1} cm^{-1})]: 341 (3.5), 394 (5.15), 521 (1.3), 539 (1.4). HRMS (major isotopomer; $[M]^+$): 655.1690 (expt), 655.1689 (calc).

Synthesis of Mn[T*p*CF$_3$PC]Ph. Silica gel column chromatography with 4:1 *n*-hexane/dichloromethane followed by PLC with 3:1 *n*-hexane/dichloromethane as the eluent afforded pure Mn[T*p*CF_3PC]Ph (0.016 g, 38%). UV−vis [CH_2Cl_2; λ_{max}, nm ($\varepsilon \times 10^{-4}$, M^{-1} cm^{-1})]: 340 (3.4), 398 (5.36), 523 (1.36), 535 (1.35). HRMS (major isotopomer; $[M]^+$): 859.1315 (expt), 859.1311 (calc).

Single-Crystal X-ray Structure Determinations. Data for all compounds were collected on beamline 11.3.1 at the Advanced Light Source, Lawrence Berkeley National Laboratory. The samples were mounted on MiTeGen Kapton loops and placed in a 100(2) K nitrogen cold stream provided by an Oxford Cryostream 700 Plus low-temperature apparatus on the goniometer head of a Bruker D8 diffractometer equipped with a PHOTON100 CMOS detector (for Mn[T*p*OMePC]Ph) or a PHOTONII CPAD detector (for the other compounds) operating in shutterless mode. Diffraction data were collected using synchrotron radiation monochromated using Si(111). Approximate full-spheres of data were collected using a combination of φ and ω scans. The crystals of Mn[T*p*CF_3PC]Cl were found to be twinned, and the components were separated using *CELL_NOW*.[55] Absorption corrections were applied using *SADABS*[56] or *TWINABS*[57] (for Mn[T*p*CF_3PC]Cl). The structures were solved by direct methods (*SHELXS*[58] for Mn[TPC]Cl) or intrinsic phasing (*SHELXT*[59]) and refined by full-matrix least squares on F^2 (*SHELXL-2014*[60]) using the *ShelXle GUI*.[61] Appropriate scattering factors were applied using the *XDISP*[62] program within the *WinGX* suite.[63] All non-H atoms were refined anisotropically. H atoms were geometrically calculated and refined as riding atoms. The Mn[TPC]Cl crystal was found to be twinned using the *TWINROTMAT* routine in *PLATON*,[64] and the appropriate twin law was added to the model. The large residual peak of the electron density in Mn[T*p*CF_3PC]$(py)_2$ was identified as the Mn site of a second orientation of the corrole unit, whose occupancy was refined to 6% (see the CIF files for additional details). Additional crystallographic information has been summarized in Table 2, and full details can be found in the CIF files.

Mn K-Edge XAS Measurements. The Mn K-edge X-ray absorption spectra of Mn[T*p*CF_3PC]Cl, Mn[T*p*CF_3PC]Ph, and Mn[T*p*CF_3PC]$(py)_n$ were measured at the SSRL on the wiggler BL9-3 under standard ring conditions of 3 GeV and ∼500 mA. A Si(220) double-crystal monochromator was used for energy selection. A harmonic rejection mirror was used and the monochromator detuned by 10% to reject components of higher harmonics. During data collection, the samples were maintained at a constant temperature of ∼10 K using an Oxford liquid-helium cryostat. Mn K-edge XAS data for Mn[T*p*CF_3PC]Cl and Mn[T*p*CF_3PC]Ph were measured in transmission mode using ion chambers as detectors. A 100-element germanium fluorescence detector from Canberra Industries was employed for fluorescence data measurements on Mn[T*p*CF_3PC]$(py)_n$. For fluorescence measurements, the background signal was suppressed using soller slits equipped with a chromium filter. The solid samples were ground to a homogeneous powder in a BN matrix. The homogeneous mixture was then placed in aluminum spacers and wrapped in Kapton tape. Solution samples were transferred into 2 mm Delrin XAS cells with 70 mm Kapton tape windows and immediately frozen after preparation and stored under liquid N_2. Internal energy calibration was accomplished by simultaneous measurement of the absorption of a manganese foil placed between two ionization chambers situated after the sample. The first inflection point of the foil spectrum was set at 6539.0 eV. The data presented here are 3-, 2-, and 12-scan average spectra for Mn[T*p*CF_3PC]Cl, Mn[T*p*CF_3PC]Ph, and Mn[T*p*CF_3PC]$(py)_n$, respectively. At least two sweeps were collected to ensure that no radiation damage was observed. Energy calibration, background correction, data averaging, and normalization were carried out with *ATHENA*, which is part of the *Demeter* software package, version 0.9.24.[65]

DFT/TDDFT Calculations. DFT geometry optimizations were carried out with the BP86 functional and a spin-unrestricted formalism, allowing for broken-symmetry solutions, using the *ORCA 3.0.3* program system.[66,67] Ahlrich's all-electron triple-ζ triple polarization TZVPPP basis set was used for the Mn atom, and TZVPP was used for all other atoms.[68] All calculations were performed in a dielectric continuum using the conductor-like screening model with benzene as the solvent.[69] Tight self-consistent-field (SCF) convergence criteria were employed throughout. The SlowConv criterion was employed. An SCF grid of 4 with no final grid was used. A higher grid (grid 7) was used on the Mn atom. The optimized structures were used for single-point calculations using the B3LYP functional (while otherwise maintaining the same calculational parameters). Subsequently, B3LYP TDDFT calculations were performed to simulate the Mn K pre-edge region (as implemented in the *ORCA* package). The number of roots was set at 20, MaxDim was set at 200, "doQuad True" was selected, and spin-flip transitions were not calculated. The TDDFT calculations were performed over the entire valence manifold and for both the spin-up (OrbWin = 0) and spin-down (OrbWin = 1) transitions. The calculated energies and intensities were broadened using the line-broadening script within *ORCA* to achieve half-widths of 1.5 eV to account for the core−hole lifetime and instrument broadening. The calculated pre-edge energies were linearly upshifted by 168.2 eV for comparison with the experimental spectra.

■ ASSOCIATED CONTENT

Ⓢ Supporting Information

The Supporting Information is available free of charge on the ACS Publications website at DOI: 10.1021/acs.inorgchem.8b00537.

EXAFS data, ESI-MS spectra, and details of DFT/TDDFT calculations (PDF)

Accession Codes

CCDC 1826554−1826558 contain the supplementary crystallographic data for this paper. These data can be obtained free of charge via www.ccdc.cam.ac.uk/data_request/cif, or by emailing data_request@ccdc.cam.ac.uk, or by contacting The Cambridge Crystallographic Data Centre, 12 Union Road, Cambridge CB2 1EZ, UK; fax: +44 1223 336033.

■ AUTHOR INFORMATION

Corresponding Authors

*E-mail: ritis@slac.stanford.edu (R.S.).
*E-mail: abhik.ghosh@uit.no (A.G.).

ORCID

Laura J. McCormick: 0000-0002-6634-4717
Jeanet Conradie: 0000-0002-8120-6830
Abhik Ghosh: 0000-0003-1161-6364

Notes

The authors declare no competing financial interest.

■ ACKNOWLEDGMENTS

This work was supported by grants 231086 and 262229 of the Research Council of Norway (AG) and the National Research Fund of the Republic of South Africa (JC). This research used resources of the Advanced Light Source, which is a DOE Office of Science User Facility under contract no. DE-AC02-05CH11231. The SSRL Structural Molecular Biology (SMB) resource is supported by the NIH National Institute of General Medical Sciences (NIGMS) through a Biomedical Technology Research Resource P41 grant (P41GM103393) and by the DOE Office of Biological and Environmental Research.

■ REFERENCES

(1) Steene, E.; Wondimagegn, T.; Ghosh, A. Electrochemical and Electronic Absorption Spectroscopic Studies of Substituent Effects in Iron(IV) and Manganese(IV) Corroles. Do the Compounds Feature High-Valent Metal Centers or Noninnocent Corrole Ligands? Implications for Peroxidase Compound I and II Intermediates. *J. Phys. Chem. B* **2001**, *105*, 11406−11413.

(2) Wasbotten, I. H.; Wondimagegn, T.; Ghosh, A. Electronic Absorption, Resonance Raman, and Electrochemical Studies of Planar and Saddled Copper(III) *Meso*-Triarylcorroles. Highly Substituent-Sensitive Soret Bands as a Distinctive Feature of High-Valent Transition Metal Corroles. *J. Am. Chem. Soc.* **2002**, *124*, 8104−8116.

(3) Brückner, C.; Briñas, R. P.; Krause Bauer, J. A. X-ray Structure and Variable Temperature NMR Spectra of [*meso*-Triarylcorrolato]-copper(III). *Inorg. Chem.* **2003**, *42*, 4495−4497.

(4) Ou, Z.; Shao, J.; Zhao, H.; Ohkubo, K.; Wasbotten, I. H.; Fukuzumi, S.; Ghosh, A.; Kadish, K. M. Spectroelectrochemical and ESR Studies of Highly Substituted Copper Corroles. *J. Porphyrins Phthalocyanines* **2004**, *8*, 1236−1247.

(5) Bröring, M.; Bregier, F.; Cónsul Tejero, E.; Hell, C.; Holthausen, M. C. Revisiting the Electronic Ground State of Copper Corroles. *Angew. Chem., Int. Ed.* **2007**, *46*, 445−448.

(6) Alemayehu, A. B.; Gonzalez, E.; Hansen, L. K.; Ghosh, A. Copper Corroles Are Inherently Saddled. *Inorg. Chem.* **2009**, *48*, 7794−7799.

(7) Alemayehu, A. B.; Hansen, L. K.; Ghosh, A. Nonplanar, Noninnocent, and Chiral: A Strongly Saddled Metallocorrole. *Inorg. Chem.* **2010**, *49*, 7608−7610.

(8) Thomas, K. E.; Wasbotten, I. H.; Ghosh, A. Copper β-Octakis(Trifluoromethyl)Corroles: New Paradigms for Ligand Substituent Effects in Transition Metal Complexes. *Inorg. Chem.* **2008**, *47*, 10469−10478.

(9) Berg, S.; Thomas, K. E.; Beavers, C. M.; Ghosh, A. Undecaphenylcorroles. *Inorg. Chem.* **2012**, *51*, 9911−9916.

(10) Thomas, K. E.; Vazquez-Lima, H.; Fang, Y.; Song, Y.; Gagnon, K. J.; Beavers, C. M.; Kadish, K. M.; Ghosh, A. Ligand Noninnocence in Coinage Metal Corroles: A Silver Knife-Edge. *Chem. - Eur. J.* **2015**, *21*, 16839−16847.

(11) Thomas, K. E.; McCormick, L. J.; Carrié, D.; Vazquez-Lima, H.; Simonneaux, G.; Ghosh, A. Halterman Corroles and Their Use as a Probe of the Conformational Dynamics of the Inherently Chiral Copper Corrole Chromophore. *Inorg. Chem.* **2018**, *57*, 4270−4276.

(12) Ghosh, A. Electronic Structure of Corrole Derivatives: Insights from Molecular Structures, Spectroscopy, Electrochemistry, and Quantum Chemical Calculations. *Chem. Rev.* **2017**, *117*, 3798−3881.

(13) Liu, H.-Y.; Mahmood, M. H. R.; Qiu, S.-X.; Chang, C. K. Recent Developments in Manganese Corrole Chemistry. *Coord. Chem. Rev.* **2013**, *257*, 1306−1333.

(14) Golubkov, G.; Bendix, J.; Gray, H. B.; Mahammed, A.; Goldberg, I.; DiBilio, A. J.; Gross, Z. High-Valent Manganese Corroles and the First Perhalogenated Metallocorrole Catalyst. *Angew. Chem., Int. Ed.* **2001**, *40*, 2132−2134.

(15) Johansen, I.; Norheim, H.-K.; Larsen, S.; Alemayehu, A. B.; Conradie, J.; Ghosh, A. Substituent Effects on Metallocorrole Spectra: Insights from Chromium-Oxo and Molybdenum-Oxo Triarylcorroles. *J. Porphyrins Phthalocyanines* **2011**, *15*, 1335−1344.

(16) Einrem, R. F.; Gagnon, K. J.; Alemayehu, A. B.; Ghosh, A. Metal-Ligand Misfits: Facile Access to Rhenium-Oxo Corroles by Oxidative Metalation. *Chem. - Eur. J.* **2016**, *22*, 517−520.

(17) Alemayehu, A. B.; Gagnon, K. J.; Terner, J.; Ghosh, A. Oxidative Metalation as a Route to Size-Mismatched Macrocyclic Complexes: Osmium Corroles. *Angew. Chem., Int. Ed.* **2014**, *53*, 14411−14414.

(18) Alemayehu, A. B.; Ghosh, A. Gold Corroles. *J. Porphyrins Phthalocyanines* **2011**, *15*, 106−110.

(19) Rabinovich, E.; Goldberg, I.; Gross, Z. Gold(I) and Gold(III) Corroles. *Chem. - Eur. J.* **2011**, *17*, 12294−12301.

(20) Thomas, K. E.; Alemayehu, A. B.; Conradie, J.; Beavers, C.; Ghosh, A. Synthesis and Molecular Structure of Gold Triarylcorroles. *Inorg. Chem.* **2011**, *50*, 12844−12851.

(21) Thomas, K. E.; Beavers, C. M.; Ghosh, A. Molecular Structure of a Gold β-Octakis(trifluoromethyl)-*meso*-Triarylcorrole: An 85° Difference in Saddling Dihedral Relative to Copper. *Mol. Phys.* **2012**, *110*, 2439−2444.

(22) Vazquez-Lima, H.; Norheim, H. K.; Einrem, R. F.; Ghosh, A. Cryptic Noninnocence: FeNO Corroles in a New Light. *Dalton Trans.* **2015**, *44*, 10146−10151.

(23) Ganguly, S.; Vazquez-Lima, H.; Ghosh, A. Wolves in Sheep's Clothing: μ-Oxo-Diiron Corroles Revisited. *Chem. - Eur. J.* **2016**, *22*, 10336−10340.

(24) Ganguly, S.; Renz, D.; Giles, L. J.; Gagnon, K. J.; McCormick, L. J.; Conradie, J.; Sarangi, R.; Ghosh, A. Cobalt- and Rhodium-Corrole-Triphenylphosphine Complexes Revisited: The Question of a Noninnocent Corrole. *Inorg. Chem.* **2017**, *56*, 14788−14800.

(25) Ghosh, A.; Steene, E. High-Valent Transition Metal Centers versus Noninnocent Ligands in Metallocorroles: Insights from Electrochemistry and Implications for High-Valent Heme Protein Intermediates. *J. Inorg. Biochem.* **2002**, *91*, 423−436.

(26) Norheim, H.-K.; Capar, J.; Einrem, R. F.; Gagnon, K. J.; Beavers, C. M.; Vazquez-Lima, H.; Ghosh, A. Ligand Noninnocence in FeNO Corroles: Insights from β-Octabromocorrole Complexes. *Dalton Trans.* **2016**, *45*, 681−689.

(27) Hocking, R. K.; George, S. D.; Gross, Z.; Walker, F. A.; Hodgson, K. O.; Hedman, B.; Solomon, E. I. Fe L- and K-edge XAS of Low-Spin Ferric Corrole: Bonding and Reactivity Relative to Low-Spin Ferric Porphyrin. *Inorg. Chem.* **2009**, *48*, 1678−1688.

(28) Sarangi, R.; Giles, L. J.; Thomas, K. E.; Ghosh, A. Ligand Noninnocence in Silver Corroles: A XANES Investigation. *Eur. J. Inorg. Chem.* **2016**, *2016*, 3225−3227.

(29) Palmer, J. H.; Lancaster, K. M. Molecular Redox: Revisiting the Electronic Structures of the Group 9 Metallocorroles. *Inorg. Chem.* **2012**, *51*, 12473−12482.

(30) Ganguly, S.; Giles, L. J.; Thomas, K. E.; Sarangi, R.; Ghosh, A. Ligand Noninnocence in Iron Corroles: Insights from Optical and X-ray Absorption Spectroscopies and Electrochemical Redox Potentials. *Chem. - Eur. J.* **2017**, *23*, 15098−15106.

(31) Ghosh, A.; Wondimagegn, T.; Parusel, A. B. J. Electronic Structure of Gallium, Copper, and Nickel Complexes of Corrole. High-Valent Transition Metal Centers Versus Noninnocent Ligands. *J. Am. Chem. Soc.* **2000**, *122*, 5100−5104.

(32) Ghosh, A.; Steene, E. High-Valent Transition Metal Centers and Noninnocent Ligands in Metalloporphyrins and Related Molecules: A Broad Overview Based on Quantum Chemical Calculations. *JBIC, J. Biol. Inorg. Chem.* **2001**, *6*, 739−752.

(33) Gao, B.; Ou, Z.; Chen, X.; Huang, S.; Li, B.; Fang, Y.; Kadish, K. M. Spectroelectrochemical Characterization of *meso* Triaryl-Substituted Mn(IV), Mn(III) and Mn(II) corroles. Effect of Solvent and Oxidation State on UV-visible Spectra and Redox Potentials in Nonaqueous Media. *J. Porphyrins Phthalocyanines* **2014**, *18*, 1131−1144.

(34) Ou, Z.; Erben, C.; Autret, M.; Will, S.; Rosen, D.; Lex, J.; Vogel, E.; Kadish, K. M. Manganese(III) and Manganese(IV) Corroles: Synthesis, Spectroscopic, Electrochemical and X-ray Structural Characterization. *J. Porphyrins Phthalocyanines* **2005**, *09*, 398−412.

(35) Bröring, M.; Cordes, M.; Köhler, S. Manganese(IV) Corroles with σ-Aryl Ligands. *Z. Anorg. Allg. Chem.* **2008**, *634*, 125−130.

(36) Alemayehu, A. B.; Conradie, J.; Ghosh, A. A First TDDFT Study of Metallocorrole Electronic Spectra: Copper *meso*-Triarylcorroles Exhibit *Hyper* Spectra. *Eur. J. Inorg. Chem.* **2011**, *12*, 1857−1864.

(37) TDDFT calculations aimed at simulating the substituent sensitivity of noninnocent metallotriarylcorroles have generally not been particularly successful. Key calculated features such as the Soret and Q bands tend to be contaminated with unphysical long-range excitations from lone pairs on the para substituent X to the corrole π system. Accordingly, we have refrained from employing TDDFT calculations to model the optical spectra of MnCl and MnPh corroles.

(38) Licoccia, S.; Morgante, E.; Paolesse, R.; Polizio, F.; Senge, M. O.; Tondello, E.; Boschi, T. Tetracoordinated Manganese(III) Alkylcorrolates. Spectroscopic Studies and the Crystal and Molecular Structure of (7,13-Dimethyl-2,3,8,12,17,18-Hexaethylcorrolato)-manganese(III). *Inorg. Chem.* **1997**, *36*, 1564−1570.

(39) Shen, J.; El Ojaimi, M.; Chkounda, M.; Gros, C. P.; Barbe, J.-M.; Shao, J.; Guilard, R.; Kadish, K. M. Solvent, Anion, and Structural Effects on the Redox Potentials and UV−visible Spectral Properties of Mononuclear Manganese Corroles. *Inorg. Chem.* **2008**, *47*, 7717−7727.

(40) Fryxelius, J.; Eilers, G.; Feyziyev, Y.; Magnuson, A.; Sun, L.; Lomoth, R. Synthesis and Redox Properties of a [*meso*-Tris(4-nitrophenyl)corrolato]Mn(III) Complex. *J. Porphyrins Phthalocyanines* **2005**, *09*, 379−386.

(41) Singh, P.; Dutta, G.; Goldberg, I.; Mahammed, A.; Gross, Z. Expected and Unexpected Transformations of Manganese(III) Tris(4-nitrophenyl)corrole. *Inorg. Chem.* **2013**, *52*, 9349−9355.

(42) Bröring, M.; Hell, C.; Brandt, C. D. Iodomanganesecorrole − a Stable Mn^{IV}-I Species. *Chem. Commun.* **2007**, 1861−1862.

(43) Kumar, A.; Goldberg, I.; Botoshansky, M.; Buchman, Y.; Gross, Z. Oxygen Atom Transfer Reactions from Isolated (Oxo)manganese(V) Corroles to Sulfides. *J. Am. Chem. Soc.* **2010**, *132*, 15233−15245.

(44) Bröring, M.; Brégier, F.; Krüger, R.; Kleeberg, C. Functional Porphyrinoids from a Biomimetically Decorated Bipyrrole. *Eur. J. Inorg. Chem.* **2008**, *35*, 5505−5512.

(45) Bröring, M.; Hell, C.; Steiner, M.; Brandt, C. D. Halogenido and Pseudohalogenido Complexes of (2,3,7,8,12,13,17,18-Octaethyl-5,15-Di-*p*-tolylcorrolato)manganese(IV). *Z. Anorg. Allg. Chem.* **2007**, *633*, 1082−1086.

(46) ESI-MS studies readily revealed a manganese monopyridine adduct but under no circumstances a bispyridine adduct. These obervations may be contrasted with those on fully characterized cobalt corrole bispyridine adducts, for which the four-coordinate, monopyridine, and bispyridine adducts are all readily detectable.[47]

(47) Ganguly, S.; Conradie, J.; Bendix, J.; Gagnon, K. J.; McCormick, L. J.; Ghosh, A. Electronic Structure of Cobalt−Corrole−Pyridine Complexes: Noninnocent Five-Coordinate Co(II) Corrole−Radical States. *J. Phys. Chem. A* **2017**, *121*, 9589−9598.

(48) de Groot, F. High-Resolution X-ray Emission and X-ray Absorption Spectroscopy. *Chem. Rev.* **2001**, *101*, 1779−1808.

(49) Sarangi, R. X-ray Absorption Near-Edge Spectroscopy in Bioinorganic Chemistry: Application to $M-O_2$ systems. *Coord. Chem. Rev.* **2013**, *257*, 459−472.

(50) XANES of $Mn[TpCF_3PC](py)_n$ as a solution in (frozen) neat pyridine revealed a pre-edge of somewhat diminished intensity relative to the solid sample, indicating reduced centrosymmetry in the solution species, consistent with an increased proportion of the bispyridine adduct ($n = 2$). For a description of the EXAFS, see the Supporting Information.

(51) Fang, Y.; Ou, Z.; Kadish, K. M. Electrochemistry of Corroles in Nonaqueous Media. *Chem. Rev.* **2017**, *117*, 3377−3419.

(52) For electrochemical HOMO−LUMO gaps of closed-shell corrole derivatives, see: Simkhovich, L.; Mahammed, A.; Goldberg, I.; Gross, Z. Synthesis and Characterization of Germanium, Tin, Phosphorus, Iron, and Rhodium Complexes of Tris(pentafluorophenyl)corrole, and the Utilization of the Iron and Rhodium Corroles as Cyclopropanation Catalysts. *Chem. - Eur. J.* **2001**, *7*, 1041−1055.

(53) Koszarna, B.; Gryko, D. T. Efficient Synthesis of *meso*-Substituted Corroles in a H_2O−MeOH Mixture. *J. Org. Chem.* **2006**, *71*, 3707−3717.

(54) Use of the positive mode in ESI-MS analysis of MnCl corroles invariably led to a loss of chlorine and to the detection of $[M - Cl]^+$ as the major species.

(55) *CELL NOW: Index Twins and Other Problem Crystals*, version 2008/4; Bruker, 2016.

(56) Krause, L.; Herbst-Irmer, R.; Sheldrick, G. M.; Stalke, D. Comparison of Silver and Molybdenum Microfocus X-ray Sources for Single-Crystal Structure Determination. *J. Appl. Crystallogr.* **2015**, *48*, 3−10.

(57) *TWINABS: Bruker AXS Scaling for Twinned Crystals*, version 2012/1; Bruker, 2016.

(58) Sheldrick, G. M. A Short History of SHELX. *Acta Crystallogr., Sect. A: Found. Crystallogr.* **2008**, *64*, 112−122.

(59) Sheldrick, G. M. SHELXT-Integrated Space-Group and Crystal-Structure Determination. *Acta Crystallogr., Sect. A: Found. Adv.* **2015**, *71*, 3−8.

(60) Sheldrick, G. M. Crystal Structure Refinement with SHELXL. *Acta Crystallogr., Sect. C: Struct. Chem.* **2015**, *71*, 3−8.

(61) Hübschle, C. B.; Sheldrick, G. M.; Dittrich, B. ShelXle: A Qt Graphical User Interface for SHELXL. *J. Appl. Crystallogr.* **2011**, *44*, 1281−1284.

(62) Kissel, L.; Pratt, R. H. Corrections to Tabulated Anomalous-Scattering Factors. *Acta Crystallogr., Sect. A: Found. Crystallogr.* **1990**, *46*, 170−175.

(63) Farrugia, L. J. WinGX and ORTEP for Windows: An Update. *J. Appl. Crystallogr.* **2012**, *45*, 849−854.

(64) Spek, A. L. Structure Validation in Chemical Crystallography. *Acta Crystallogr., Sect. D: Biol. Crystallogr.* **2009**, *65*, 148−155.

(65) Ravel, B.; Newville, M. ATHENA, ARTEMIS, HEPHAESTUS: Data Analysis for X-ray Absorption Spectroscopy using IFEFFIT. *J. Synchrotron Radiat.* **2005**, *12*, 537−541.

(66) Neese, F.; Olbrich, G. Efficient use of the Resolution of the Identity Approximation in Time-Dependent Density Functional Calculations with Hybrid Density Functionals. *Chem. Phys. Lett.* **2002**, *362*, 170−178.

(67) Neese, F. *ORCA: An Ab Initio, DFT and Semiempirical SCF-MO Package*, version 3.0.3; University of Bonn: Bonn, Germany, 2016.

(68) Weigend, F.; Ahlrichs, R. Balanced Basis Sets of Split Valence, Triple Zeta Valence and Quadruple Zeta Valence Quality for H to Rn: Design and Assessment of Accuracy. *Phys. Chem. Chem. Phys.* **2005**, *7*, 3297−3305.

(69) Sinnecker, S.; Rajendran, A.; Klamt, A.; Diedenhofen, M.; Neese, F. Calculation of Solvent Shifts on Electronic g-Tensors with the Conductor-Like Screening Model (COSMO) and Its Self-Consistent Generalization to Real Solvents (Direct COSMO-RS). *J. Phys. Chem. A* **2006**, *110*, 2235−2245.

DOI: 10.1021/acs.inorgchem.8b00537